Supplemental Data

TRIOBP-5 sculpts stereocilia rootlets and stiffens supporting cells enabling hearing

Tatsuya Katsuno[1,*], Inna A. Belyantseva[2,*], Alexander X. Cartagena-Rivera[3], Keisuke Ohta[4], Shawn M. Crump[5], Ronald S. Petralia[6], Kazuya Ono[1,+], Risa Tona[1,2], Ayesha Imtiaz[2], Atteeq Rehman[2,$], Hiroshi Kiyonari[7], Mari Kaneko[7], Ya-Xian Wang[6], Takaya Abe[7], Makoto Ikeya[8], Cristina Fenollar-Ferrer[2,9], Gavin P. Riordan[2], Elisabeth Wilson[2], Tracy S. Fitzgerald[10], Kohei Segawa[1], Koichi Omori[1], Juichi Ito[1], Gregory I. Frolenkov[5], Thomas B. Friedman[2,#,] Shin-ichiro Kitajiri[1,11,#]

[1]Department of Otolaryngology-Head and Neck Surgery, Kyoto University Graduate School of Medicine, Kyoto, Japan. [2]Laboratory of Molecular Genetics, National Institute on Deafness and Other Communication Disorders, NIH, Bethesda, Maryland 20892, USA. [3]Section on Auditory Mechanics, National Institute on Deafness and Other Communication Disorders, NIH, Bethesda, Maryland, USA. [4]Advanced Imaging Research Center, Kurume University School of Medicine, Kurume, Japan. [5]Department of Physiology, University of Kentucky, Lexington, USA. [6]Advanced Imaging Core, National Institute on Deafness and Other Communication Disorders, NIH, Bethesda, Maryland, USA. [7]Laboratory for Animal Resources and Genetic Engineering, Riken Center for Biosystems Dynamics Research, Kobe, Japan. [8]Department of Clinical Application, Center for iPS Cell Research and Application, Kyoto University, Kyoto, Japan. [9]Laboratory of Molecular and Cellular Neurobiology, National Institute of Mental

Health, NIH, Bethesda, Maryland, USA. [10]Mouse Auditory Testing Core Facility, National Institute on Deafness and Other Communication Disorders, NIH, Bethesda, Maryland, USA. [11]Department of Otorhinolaryngology, Shinshu University School of Medicine, Matsumoto, Japan.

Authorship note: TK and IAB contributed equally to this work.

#Co-communicating authors

* TK and IAB contributed equally to this work

Address correspondence to: Thomas B. Friedman, National Institute on Deafness and Other Communication Disorders, National Institutes of Health, 1F-141 Porter Neuroscience Center, 35 Convent Drive, Bethesda, MD 20892, USA, Phone 301-496-7882, Email: friedman@nidcd.nih.gov or Shin-ichiro Kitajiri, Department of Otorhinolaryngology, Shinshu University School of Medicine, 3-1-1 Asahi, Matsumoto, Nagano 390-8621, Japan Phone: 81-263-37-2666, Email: kitajiri@shinshu-u.ac.jp

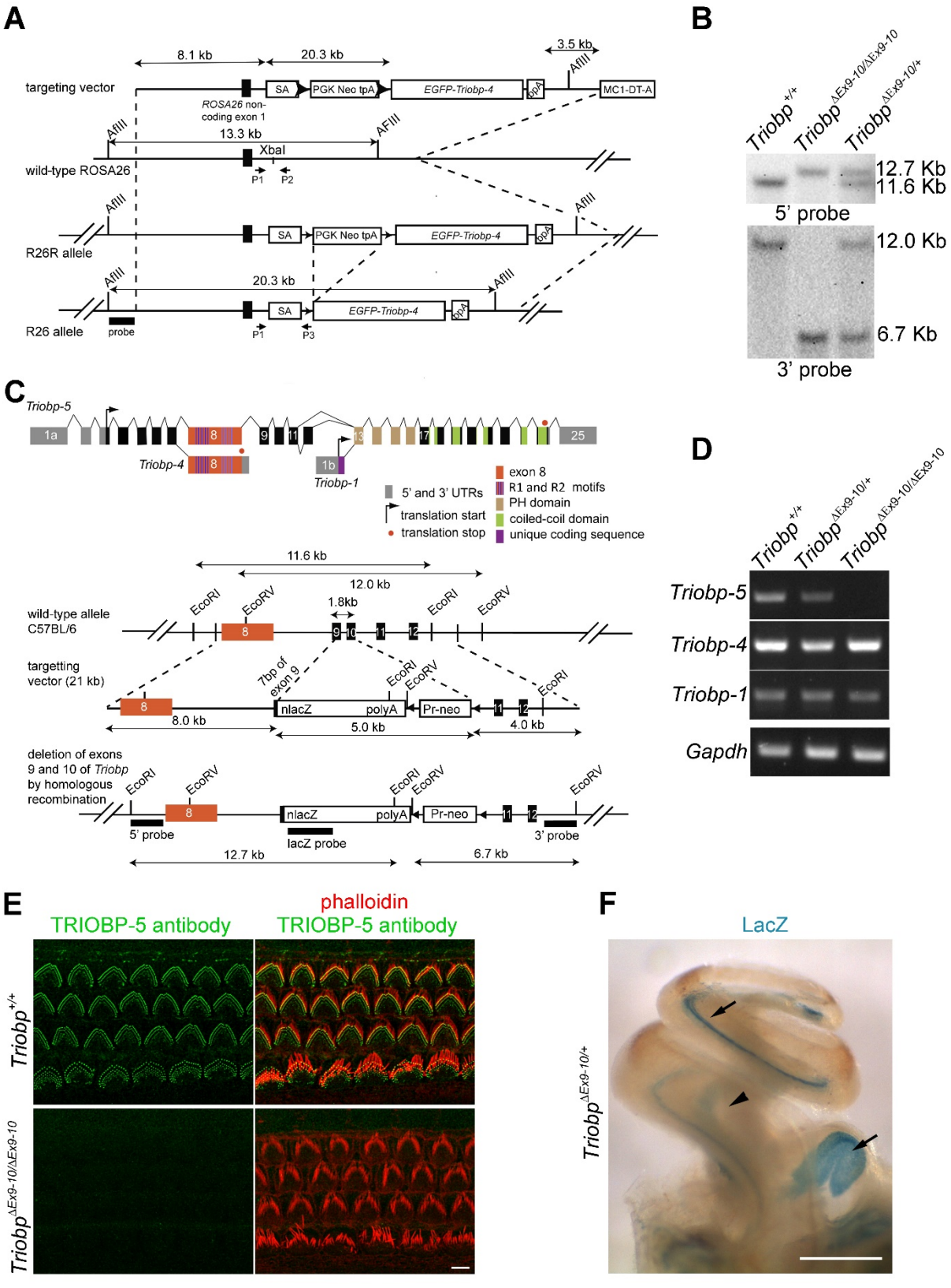

Supplemental Figure 1. (**A**) *R26-EGFP-Triobp-4* transgene reporter mouse. The

EGFP-Triobp-4 cDNA was integrated into the Rosa26 locus. P1, P2 and P3 are PCR primers for genotyping transgenic mice. SA, adenovirus splice acceptor sequence; bpA, bovine growth hormone polyadenylation sequence. (**B**) Genomic Southern blot shows that exons 9 and 10 were deleted in the *Triobp*$^{\Delta Ex9\text{-}10/\Delta Ex9\text{-}10}$ mouse. (**C**) Schematic of exon composition of *Triobp-5* isoform and targeting vector used to generate the *Triobp*$^{\Delta Ex9\text{-}10}$ mouse deleted for exons 9 and 10. (**D**) RT-PCR detection of *Triobp* isoforms in *Triobp*$^{\Delta Ex9\text{-}10}$ mice. Deletion of exons 9 and 10 eliminates expression of wild type *Triobp-5* but does not affect expression of *Triobp-4* and *Triobp-1*. (**E**) Immunostaining of the organs of Corti from P5 *Triobp*$^{+/+}$ (wild-type) and *Triobp*$^{\Delta Ex9\text{-}10/\Delta Ex9\text{-}10}$ mice, using Alexa Fluor 546- or rhodamine-phalloidin (red) to highlight F-actin and anti-TRIOBP-5 antibody (green), shows the absence of a TRIOBP-5 signal in *Triobp*$^{\Delta Ex9\text{-}10/\Delta Ex9\text{-}10}$, confirming the TRIOBP-5 deficiency and the specificity of the antibody. Scale bar is 5 μm. (**F**) LacZ staining of P13 *Triobp*$^{\Delta Ex9\text{-}10/+}$ mouse inner ear shows *Triobp-5* mRNA expression in organ of Corti and vestibular sensory epithelia (arrows) as well as in spiral ganglion neurons (arrowhead). Scale bar is 500 μm.

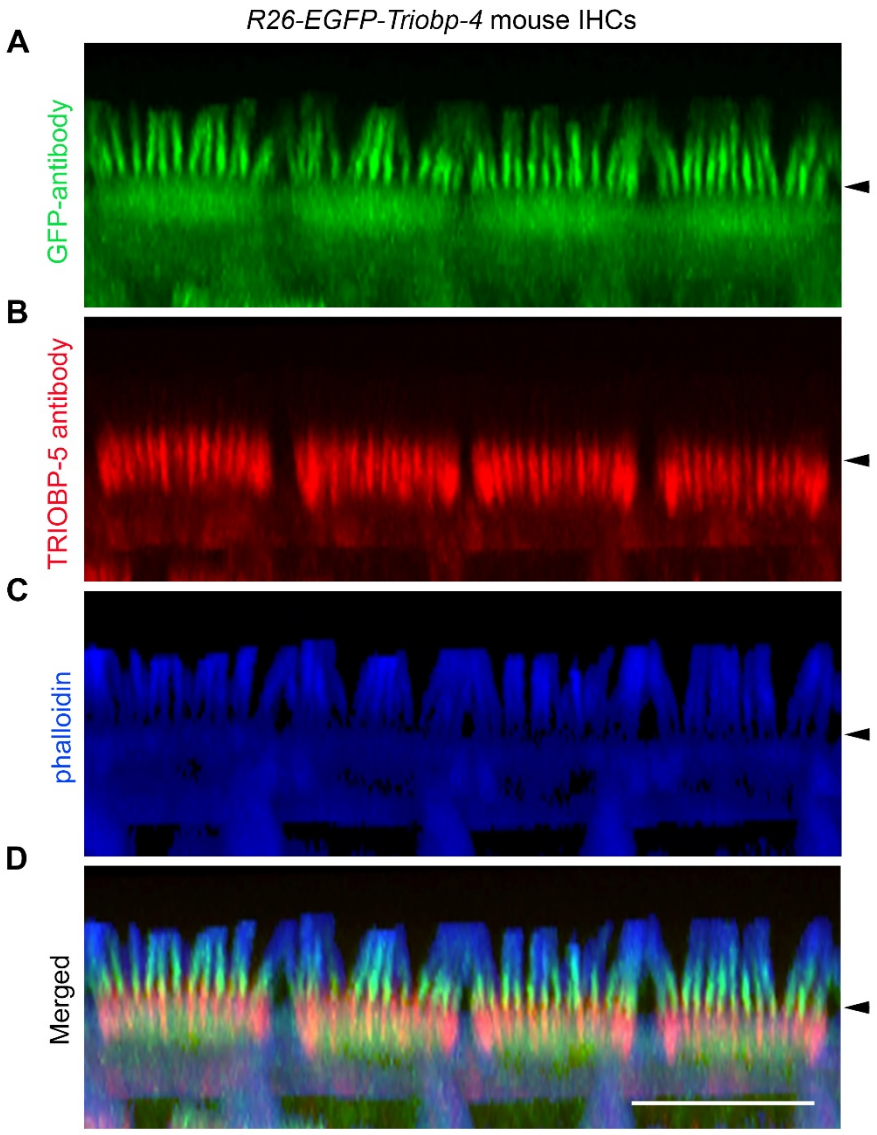

Supplemental Figure 2. Differential localization of TRIOBP-4 and TRIOBP-5 in IHCs of P18 *R26-EGFP-Triobp-4* mouse. (**A**) Anti-GFP antibody recognized EGFP-TRIOBP-4 in stereocilia rootlet segments that resides above the cuticular plate within the stereocilia core. A diffuse EGFP-TRIOBP-4 signal is present in the cuticular plate (green). (**B**) TRIOBP-5-specific antibody shows the TRIOBP-5 signal predominantly in the rootlet segments inside the cuticular plate (red). (**C**) Phalloidin-647 highlights the F-actin in the stereocilia and cuticular plates of IHCs (blue). (**D**) Merged image of panels **A**, **B** and **C**. Arrowheads indicate IHC apical surface. Scale bar is 5 μm.

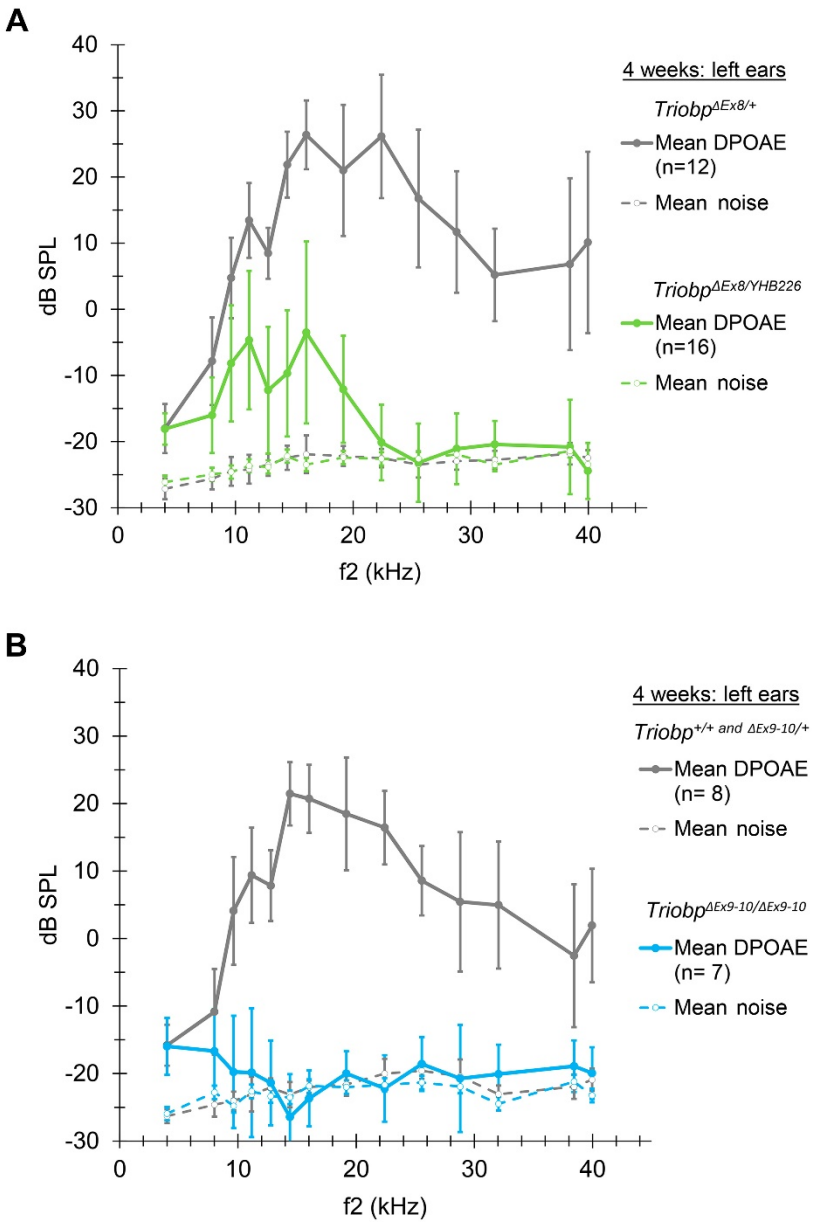

Supplemental Figure 3. (**A**) Mean DPOAEs measured in *Triobp*$^{\Delta Ex8/YHB226}$ mice and *Triobp*$^{\Delta Ex8/+}$ littermate controls. At 4 weeks of age, only weak DPOAE signals were recorded in 9 of the 16 *Triobp*$^{\Delta Ex8/YHB226}$ mice and only within the range of 8-20 kHz. No DPOAEs are detected above 20 kHz in any of these mice. Error bars indicate SD. (**B**) DPOAEs of 4-week-old *Triobp*$^{\Delta Ex9-10/\Delta Ex9-10}$ mice and littermate controls. One of the

seven *Triobp*$^{\Delta Ex9\text{-}10/\Delta Ex9\text{-}10}$ mice had low but detectable DPOAEs from 8-11.2 kHz; otherwise, DPOAEs were absent. Mean noise floors were calculated using six samples, three on either side of the DPOAE frequency, for all mice and are indicated by the dashed lines. Error bars indicate SD.

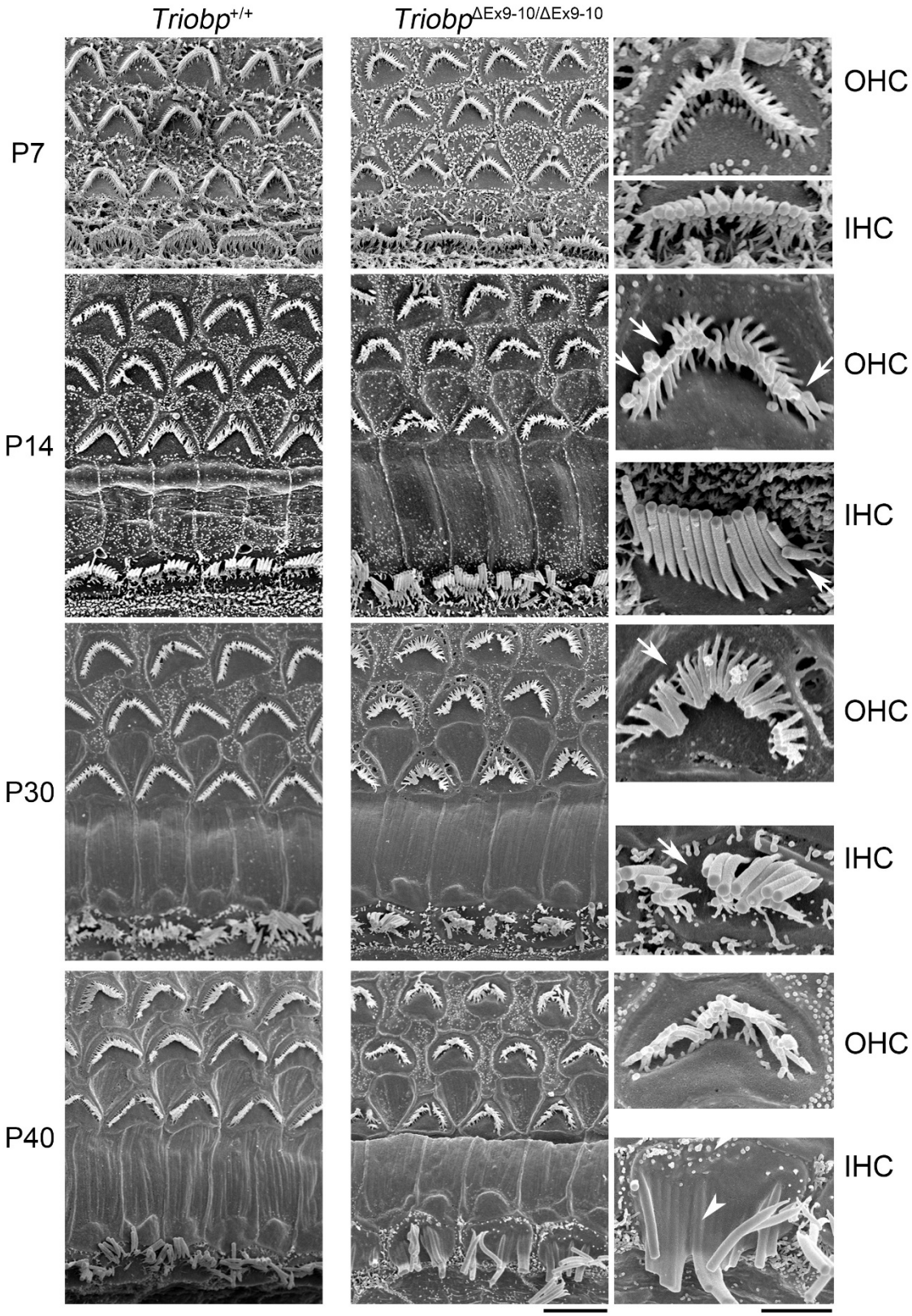

Supplemental Figure 4. Progressive degeneration of stereocilia bundles in TRIOBP-5

deficient mice (*Triobp*$^{\Delta Ex9\text{-}10/\Delta Ex9\text{-}10}$). SEM images of mouse stereocilia bundles in *Triobp*$^{+/+}$ (wild-type) (left) and *Triobp*$^{\Delta Ex9\text{-}10/\Delta Ex9\text{-}10}$ (middle) organs of Corti at P7, P14, P30 and P40 (from top to bottom). Higher magnification images of IHC and OHC bundles of mutant hair cells are shown on the right to visualize stereocilia abnormalities such as missing stereocilia starting at P14 (arrows) and stereocilia fusion evident at P40 (arrowhead). Scale bars: 5 μm (left and middle panels) and 2 μm (right panels).

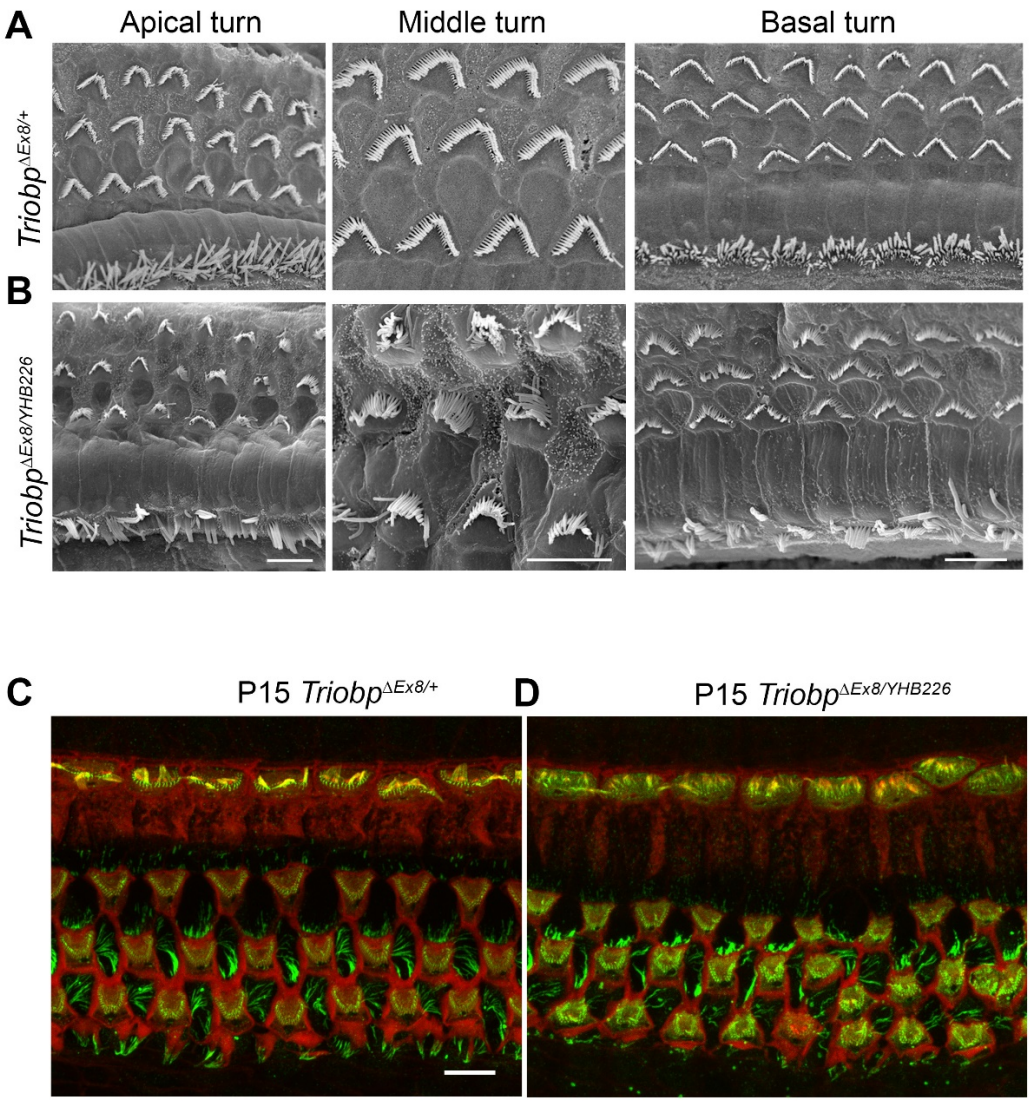

Supplemental Figure 5. SEM images of P43 *Triobp*$^{\Delta Ex8/+}$ (**A**) and *Triobp*$^{\Delta Ex8/YHB226}$ (**B**) hair cell stereocilia bundles. Note disorganization, loss of rigidity and fusion of TRIOBP-5 deficient stereocilia of *Triobp*$^{\Delta Ex8/YHB226}$ compound heterozygous hair bundles. Some OHCs are missing. Scale bars: 5 μm. TRIOBP-4/5 specific antibodies show presence of stereocilia rootlets (green) in P15 *Triobp*$^{\Delta Ex8/+}$ hair cells (**C**), and *Triobp*$^{\Delta Ex8/YHB226}$ hair cells (**D**) from the middle turn of the organ of Corti. In both panels, F-actin is visualized with rhodamine-phalloidin (red), and the images are maximum intensity projections of corresponding confocal Z-stacks. Scale bars: 5 μm.

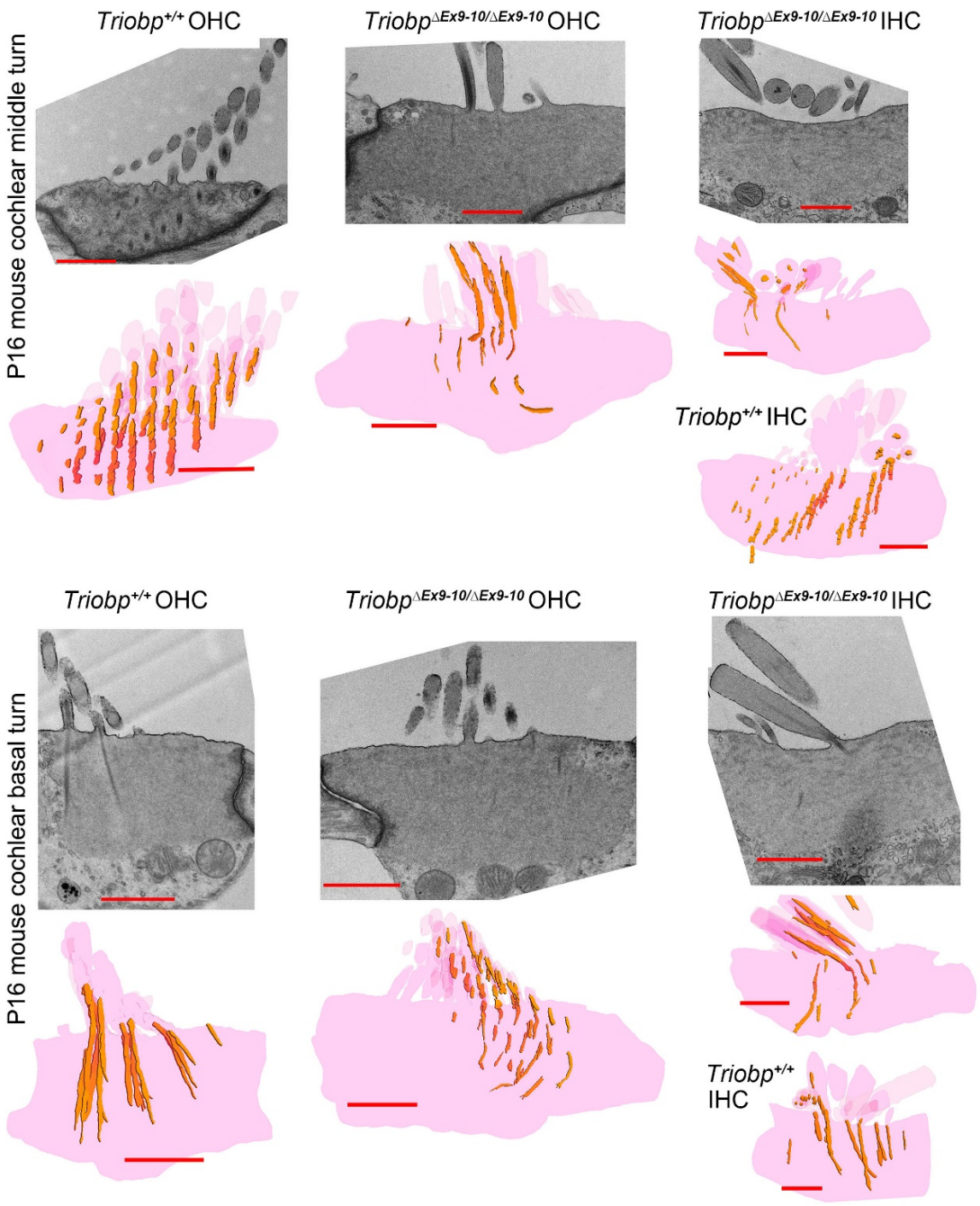

Supplemental Figure 6. Reconstructions of images from serial TEM sections of stereocilia of hair cells from P16 mice. Note the irregular and reduced or attenuated rootlets in the *Triobp*$^{\Delta Ex9\text{-}10/\Delta Ex9\text{-}10}$ mouse, compared to those in the wild-type *Triobp*$^{+/+}$ mouse. Examples are from middle (top row) and basal turns (bottom row). Examples from the apical turn are shown in Figure 4. The 3D reconstructions (rootlets colored

orange) are accompanied by a representative image from the serial sections (each ~60 nm thick). Reconstructions in the top row: *Triobp*$^{+/+}$ OHC from 10 serial sections; *Triobp*$^{\Delta Ex9\text{-}10/\Delta Ex9\text{-}10}$ OHC from 10 of 11 serial sections; *Triobp*$^{+/+}$ IHC from 10 serial sections; *Triobp*$^{\Delta Ex9\text{-}10/\Delta Ex9\text{-}10}$ IHC from 11 serial sections. Reconstructions in the bottom row: *Triobp*$^{+/+}$ OHC from 8 serial sections; *Triobp*$^{\Delta Ex9\text{-}10/\Delta Ex9\text{-}10}$ OHC from 12 serial sections; *Triobp*$^{\Delta Ex9\text{-}10/\Delta Ex9\text{-}10}$ IHC from 11 serial sections; *Triobp*$^{+/+}$ IHC from 7 of 8 serial sections. Differences between *Triobp*$^{+/+}$ and *Triobp*$^{\Delta Ex9\text{-}10/\Delta Ex9\text{-}10}$ rootlets appear to be more prominent in apical and middle turns, compared to basal turns. Note that all of these reconstructions include only a portion of the stereocilia bundle.

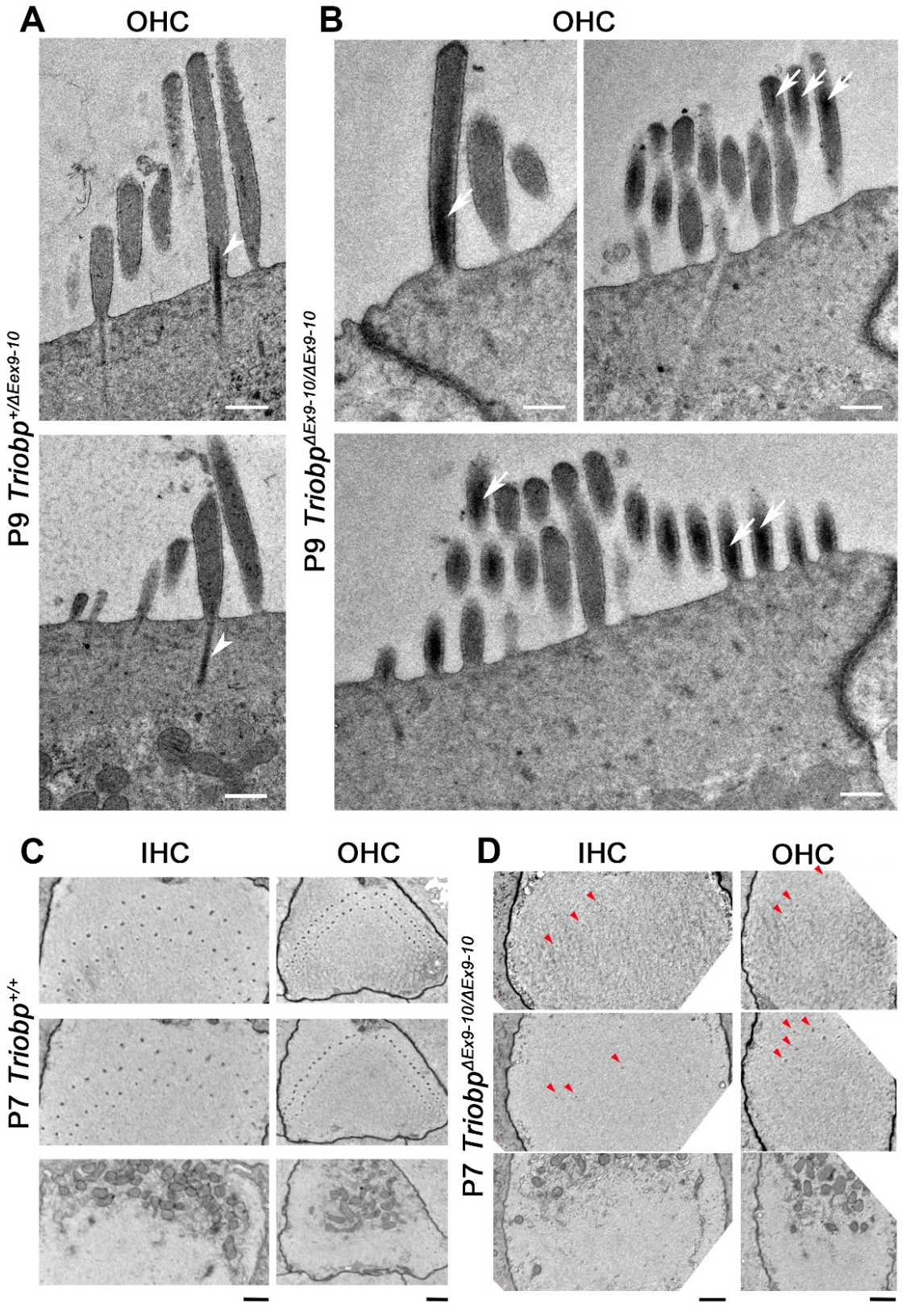

Supplemental Figure 7. Stereocilia rootlet abnormalities of P7 and P9 *Triobp*$^{Ex9\text{-}10/\Delta Ex9\text{-}}$

^{10} OHCs and IHCs. Sagittal section images through the hair bundles and cuticular plates of the OHCs from middle turn of the cochlea of P9 *Triobp*$^{+/\Delta Ex9\text{-}10}$ (**A**) and *Triobp*$^{Ex9\text{-}10/\Delta Ex9\text{-}10}$ (**B**) mice. Wild-type compact rootlets are visible in *Triobp*$^{+/\Delta Ex9\text{-}10}$ control stereocilia (arrowheads), while *Triobp*$^{Ex9\text{-}10/\Delta Ex9\text{-}10}$ stereocilia show wider rootlets that extend to the tips of some stereocilia (arrows). Transverse sections at three different levels through cuticular plate depth showing stereocilia rootlets of IHCs and OHCs from the middle turn of the cochlea of P7 *Triobp*$^{+/+}$ (**C**) and *Triobp*$^{Ex9\text{-}10/\Delta Ex9\text{-}10}$ (**D**) mice. The rootlets within the cuticular plate of wild-type control mice are clearly evident at P7 (rows of dark grey spots). Rootlets within the cuticular plate of the *Triobp*$^{Ex9\text{-}10/\Delta Ex9\text{-}10}$ mice at P7 are not as evident (red arrowheads). Scale bars; **A** and **B**: 200 nm; **C** and **D**: 500 nm.

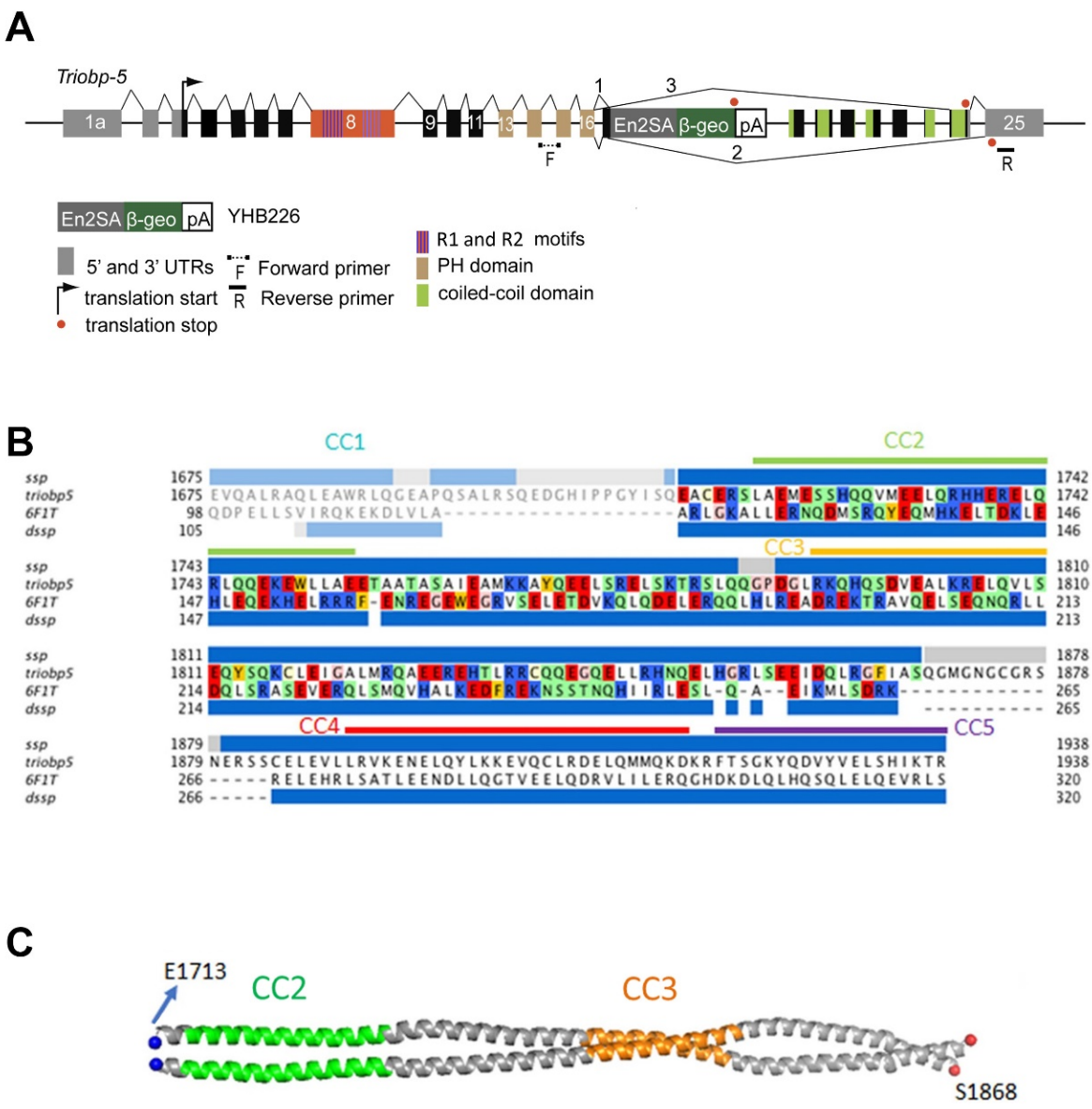

Supplemental Figure 8. Structural model of TRIOBP-5 coiled-coil domains. (**A**) Schematic of the exon composition and functional domain showing splicing of a short *Triobp-5* transcript that excludes exon 17 and the location of the YHB226 trap-cassette. Forward (F) and reverse (R) primers complimentary to sequence at the junction of exons 14-15 and a sequence within exon 25 are shown under the schematic. These primers PCR amplified a cDNA encoding exon 15 spliced directly to exons 24-25, a transcript that excludes the sequence encoding coiled-coil domains and the YHB226

trap-cassette in exon 17. (**B**) Sequence alignment between the C-terminal domain of mouse TRIOBP-5 (residues 1675-1938, accession # ABB59557) and the coiled-coil domains of the activating adaptor of the dynein-dynactin microtubule motor BICDR1 (chain X from PDBid: 6F1T) was used as template during the modelling process. Segments in the alignment used to obtain the structural model of TRIOBP-5 are highlighted, while those not used in the modelling are in muted colors. The secondary structure evident in the X-ray of 6F1T and predicted in the case of TRIOBP-5 is shown as blue and gray bars, indicating helical and coiled segments, respectively. (**C**) Structural model of the dimer comprising the coiled-coil domains 2 and 3 of mouse TRIOBP-5 (resides 1713-1868). The two chains are shown in green and orange. N- and C-terminal residues are indicated as blue and red spheres, respectively.

Methods

Molecular modelling of TRIOBP-5 coiled-coil domains 2 and 3. Template-based molecular modelling is key to identify an X-ray structure to serve as template for the modelling process. A sensitive method for template detection (1-3) uses Hidden-Markov sequence profiles (HMMs) containing a set of aligned homologs and their predicted-averaged secondary structure. The profile was obtained with HHblits after three iterations against the UniProt20 database (November 2017) and was then used as input in the HMM profiles corresponding to every single X-ray structure present in the protein data bank (PDB). The X-ray structure corresponding to the dimer of the activating adaptor BICDR1 forming part of a microtubule motor complex (PDBid: 6F1T) showed the best correspondence between secondary structural elements and therefore was

selected as the most suitable template of mouse TRIOBP-5 (accession ABB59557). The initial sequence alignment obtained covered coiled-coil domains 3-5 from mouse TRIOBP-5, residues 1675-1938 of mouse TRIOBP-5 and 98-320 of mouse BICDR1 (accession # A0JNT9), but the presence of a large number of gaps in the helical segments corresponding to coiled-coil domains 4 and 5 introduced structural distortions in the helix pattern in the resulting model of TRIOBP, and therefore coiled-coil domains 4 and 5 were excluded from the modelling procedure (Supplemental Figure 8 above). The alignment containing residues 1713-1868 (mouse TRIOBP-5) of coiled-coil domains 2,3 and 117-265 (BICDR1) was used for the final run where a pool of 2000 models was generated with Modeller (4). The final selected model of TRIOBP-5 had the highest MolPDF score and best PROCHECK (5) analysis.

1. Hildebrand A, Remmert M, Biegert A, and Soding J. Fast and accurate automatic structure prediction with HHpred. *Proteins.* 2009;77 Suppl 9:128-132.
2. Zimmermann L, Stephens A, Nam SZ, Rau D, Kubler J, Lozajic M, et al. A completely reimplemented MPI bioinformatics toolkit with a new HHpred server at its core. *J Mol Biol.* 2018;430(15):2237-2243.
3. Remmert M, Biegert A, Hauser A, and Soding J. HHblits: lightning-fast iterative protein sequence searching by HMM-HMM alignment. *Nat Methods.* 2011;9(2):173-175.
4. Webb B, and Sali A. Comparative protein ptructure modeling using MODELLER. *Curr Protoc Bioinformatics.* 2016;54:561-5637.
5. Laskowski RA, MacArthur MW, Mioss DS, and Thornton JM. PROCHECK: A program to check the stereochemical quality of proteinn structures. *J Appl Cryst.* 1993;26:283-291.

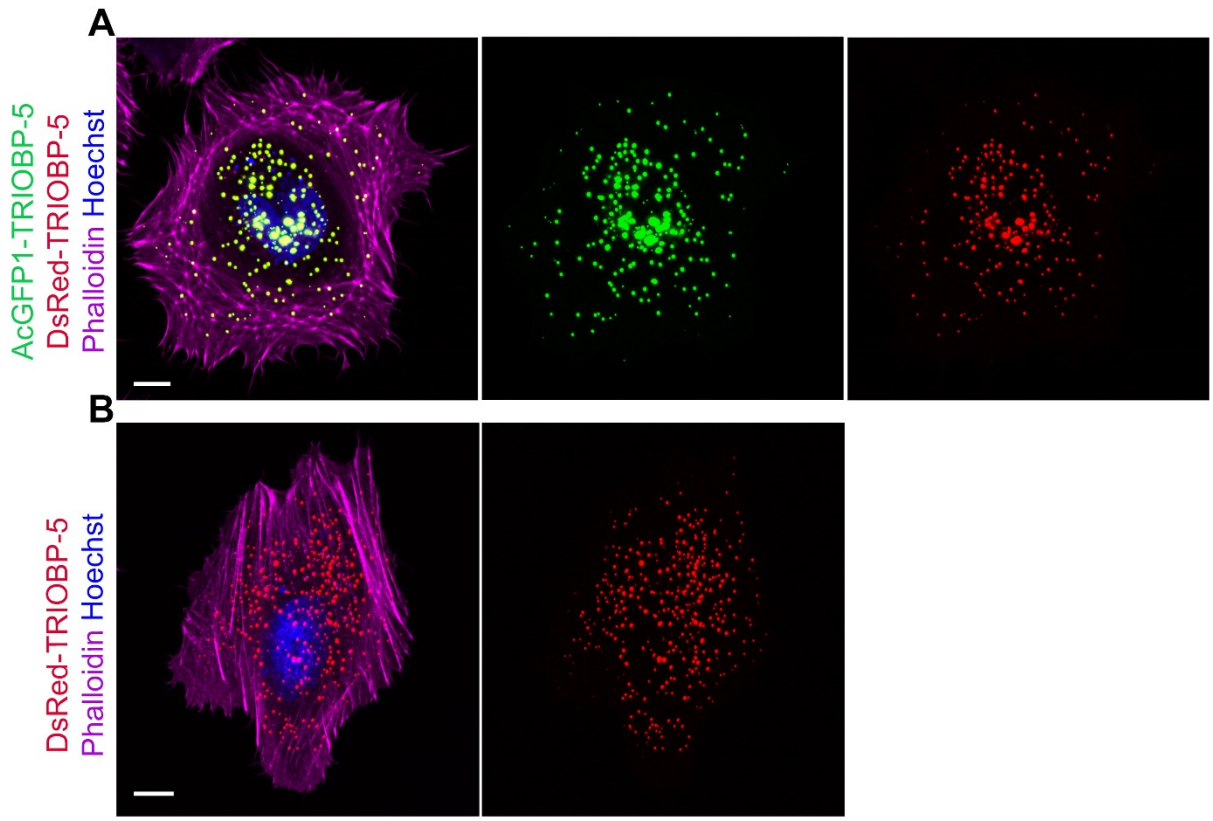

Supplemental Figure 9. Additional controls for data in Figure 7 showing expression of transfected HeLa cells with DsRed-TRIOBP-5. (**A**) Transfected expression vectors for AcGFP1-TRIOBP-5 and DsRed-TRIOBP-5 show colocalization only in the cell body. (**B**) Expression of DsRed-TRIOBP-5 alone is not localized at filopodia tips. Scale bars: 10 μm.

Supplemental Table 1. Supporting cell apical surface elastic Young's modulus, "stiffness", of the organ of Corti middle turn from live P5 mice.

Supporting cells	Number of cells	Mean (kPa)	SD (kPa)
IPC *Triobp-5*$^{\Delta Ex9\text{-}10/+}$	41	19.8	7.7
IPC *Triobp-5*$^{\Delta Ex9\text{-}10/\Delta Ex9\text{-}10}$	22	11.2	4.1
OPC *Triobp-5*$^{\Delta Ex9\text{-}10/+}$	55	27.7	11
OPC *Triobp-5*$^{\Delta Ex9\text{-}10/\Delta Ex9\text{-}10}$	46	17.6	5.8
DC1 *Triobp-5*$^{\Delta Ex9\text{-}10/+}$	53	39.8	13.2
DC1 *Triobp-5*$^{\Delta Ex9\text{-}10/\Delta Ex9\text{-}10}$	60	21.6	6.2
DC2 *Triobp-5*$^{\Delta Ex9\text{-}10/+}$	28	46	19.2
DC2 *Triobp-5*$^{\Delta Ex9\text{-}10/\Delta Ex9\text{-}10}$	32	25.4	7.4

*IPC, Inner pillar cells; OPC, Outer pillar cells; DC1, Deiters' cells 1; and DC2, Deiters' cells 2. Represented data were acquired in replicates for *Triobp-5*$^{\Delta Ex9\text{-}10/+}$ heterozygous mice (gray, 5 animals) and *Triobp-5*$^{\Delta Ex9\text{-}10/\Delta Ex9\text{-}10}$ homozygous mice (purple, 4 animals).

Supplemental video 1 legend: Orthoslices and 3D reconstruction from the correlative FIB-SEM dataset (see Figure 5I-L) showing the OHC of P14 *Triobp*$^{\Delta Ex9\text{-}10/+}$ mouse. The rootlets (yellow and orange) and stereocilia (blue) are false-colored to improve visualization.

Supplemental video 2 legend: Orthoslices and 3D reconstruction from the correlative FIB-SEM dataset (see Figure 5M-P) showing the OHC of a P14 *Triobp*$^{\Delta Ex9\text{-}10/\Delta Ex9\text{-}10}$ mouse. Rootlets (yellow and orange) and stereocilia (blue) are false-colored to improve visualization.

Supplemental video 3 legend: A side-by-side montage of two representative video recordings of IHC bundle deflections evoked by fluid-jet stimuli of increasing intensities (as in Figure 8D, inset) in *Triobp*$^{+/+}$ (wild-type) (left) and *Triobp*$^{\Delta Ex9\text{-}10/\Delta Ex9\text{-}10}$ (right) mice.